nature communications

Article

https://doi.org/10.1038/s41467-025-59720-3

Large thermoelastic effect in martensitic phase of ferroelastic alloys for high efficiency heat pumping

Received: 3 October 2024

Accepted: 30 April 2025

Qiao Li[1], Zhongzheng Deng[1], Aslan Ahadi[2,3], Kangjie Chu[4], Jie Yan[5], Kai Huang[6], Sixia Hu[7], Yang Ren[5], Binbin He[8] & Qingping Sun[1,9]

Solid state heat pumping using latent heat from first order ferroic phase transitions is a promising green alternative to traditional vapor compression technology. However, the intrinsic phase transition hysteresis poses a limitation on heat pumping energy efficiency. Here, we propose heat pumping using reversible heat from anhysteretic elastic deformation in martensitic phase of ferroelastic alloys. Conventionally, this thermoelastic effect (TeE) is considered too weak to be practical. But we find that in [100]-textured $Ti_{78}Nb_{22}$ martensitic polycrystals, the TeE can produce a large adiabatic temperature change (ΔT_{ad}) of 4–5 K at 413–473 K due to macroscopic large linear thermal expansion ($\alpha_l = 10^{-4}$/K). This large TeE not only far exceeds those of ordinary metals ($\Delta T_{ad} \approx 0.2K$) but also brings a material-level energy efficiency that reaches about 90% of the Carnot theoretical limit. In other ferroelastic martensitic alloys with larger intrinsic α_l (up to 5.4×10^{-4}/K), the TeE is predicted to bring an even larger ΔT_{ad} (up to 22 K) while maintaining relatively high efficiency. Our findings offer a non-phase-transition-based way for high efficiency solid state heat pumping.

About half of the energy produced globally is consumed for heating[1,2]. This involves district heating (usually below 353 K) in the building sector and process heating (mostly within 373–503 K) in industrial sectors[3,4]. At present, the global heat demand is still dominantly supplied by burning fossil fuels, which is both emission-intensive and energy-intensive. A more energy-efficient way is to use heat-pumping based on vapor compression (VC) as it can recover industrial waste heat or ambient heat at low energy costs. However, the refrigerants used in VC heat-pumping have raised widespread concern due to their high global-warming potential[3,5]. There is an urgent demand for energy-efficient and eco-friendly heat-pumping technologies[5–7].

Among green alternatives, solid-state heat-pumping using first-order phase transition of shape memory alloys (SMAs) has attracted much attention[5,8–15]. Various high-performance heat-pumping devices have been developed using SMAs with large adiabatic temperature changes (ΔT_{ad})[6,8–11,16–18]. Nevertheless, the energy efficiency of SMAs only reaches about 50%–70% of the Carnot theoretical limit, significantly lower than those of VC-based refrigerants (~90%). Higher material-level efficiency is critical since it stands for the upper limit of the device-level energy efficiency. However, this goal is difficult to achieve in SMAs due to intrinsic hysteresis associated with the first-order phase transition[13,19]; exploring

---

[1]Department of Mechanical and Aerospace Engineering, The Hong Kong University of Science and Technology, Hong Kong, China. [2]Pasargad Institute for Advanced Innovative Solutions (PIAIS), Tehran, Iran. [3]Institute for Materials, Ruhr University Bochum, Universitätsstr. 150, 44801 Bochum, Germany. [4]Department of Materials Science and Engineering, Southern University of Science and Technology, Shenzhen, China. [5]Department of Physics, City University of Hong Kong, Hong Kong, China. [6]Department of Engineering Mechanics, Wuhan University, Wuhan, China. [7]Public Center of Analysis and Testing, Southern University of Science and Technology, Shenzhen, China. [8]State Key Laboratory of Quantum Functional Materials, Department of Mechanical and Energy Engineering, Southern University of Science and Technology, Shenzhen, China. [9]HKUST Shenzhen-Hong Kong Collaborative Innovation Research Institute, Futian, Shenzhen, China. e-mail: mezzd@ust.hk; hebb@sustech.edu.cn; meqpsun@ust.hk

anhysteretic non-phase-transition pathways may open a new way out.

In this study, we propose solid-state heat pumping using ΔT_{ad} from anhysteretic linear elastic deformation (Fig. 1(a)), or *thermoelastic effect (TeE)*, in martensitic phase of ferroelastic alloys. In physics, the TeE has long been established as a fundamental caloric effect of linear-elastic solids by Kelvin[20], Joule[21] and Duhamel[22]. Regrettably, this age-old effect is generally considered too weak ($\Delta T_{ad} \approx 0.2$ K for most metals[21,23–26]) to be practical. Efforts to enhance the TeE, especially in metals, have been scarce over the last two centuries. Here, guided by thermoelasticity theory, we discover that [100]-textured $Ti_{78}Nb_{22}$ martensitic polycrystals can exhibit a large TeE with ΔT_{ad} of 4–5 K (at 413–473 K) due to the macroscopic large linear thermal expansion ($\alpha_l = 94 \times 10^{-6}$/K). Moreover, such a large TeE brings a material-level high energy efficiency, reaching ~90% of the Carnot theoretical limit. In many other martensitic ferroelastic alloys with larger intrinsic α_l (up to 5.4×10^{-4}/K), the TeE is predicted to bring an even larger ΔT_{ad} up to 22 K in their respective martensitic temperature regions. The discovered large TeE opens the possibility for elasticity-based heat pumping, which complements the prevailing phase-transition-based ways for ecofriendly and energy-efficient heat supply.

Results

Theoretical foundation for large TeE in martensitic phase of ferroelastic alloys

According to thermoelasticity theory, the TeE of solids is related to intrinsic thermal expansion[20,27,28]. For anisotropic solids, the ΔT_{ad} upon rapid uniaxial loading can be quantified as[20,27–29]:

$$\Delta T_{ad} = -T_{amb}\frac{\sigma\alpha_l}{\lambda}, \qquad (1)$$

where T_{amb} and σ are ambient temperature and applied uniaxial stress; λ and α_l are the heat capacity per unit volume and coefficient of intrinsic linear thermal expansion (CTE) along the loading direction (see Eqs. (S1) and (S2) in Supplementary information for definition of α_l). Equation (1) can be derived from Maxwell thermodynamic relation, as demonstrated by Kelvin[20] for isotropic solids and by Biot[27] for anisotropic solids, or from the Helmholtz free energy function of linear-elastic solids, as demonstrated by Landau[28]. According to Eq. (1), at a given T_{amb} and σ, ΔT_{ad} is fully determined by the material properties of λ and α_l. Given the small difference in λ among metals, the key to a large ΔT_{ad} in metals under a moderate σ is a large intrinsic α_l, as schematically shown in Fig. 1(b).

The martensitic phase in ferroelastic alloys possesses temperature-dependent intrinsic α_l following a unique scaling law[30–33] (see explanation in Note 1 of Supplementary Information):

$$\alpha_l \propto \frac{1}{\sqrt{T_c - T_{amb}}}, \qquad (2)$$

and thus

$$\Delta T_{ad} \propto T_{amb}\alpha_l\sigma \propto \frac{T_{amb}\sigma}{\sqrt{T_c - T_{amb}}}, \qquad (3)$$

where T_c is the absolute instability temperature of the martensitic phase and can be approximated as the starting temperature (A_s point) for the martensite → austenite transition. It is seen from Eqs. (2) and (3) that the martensitic phase is expected to exhibit large α_l and consequently a large ΔT_{ad} under a moderate uniaxial stress σ near T_c.

In experiment, the scaling law in Eq. (2) is supported by the thermal-expansion data of the martensitic lattice in many ferroelastic alloys (Supplementary Figs. 1 and 2); large negative or positive CTEs that are 10 to 50 times those of common metallic materials have been observed along [100] or [001] crystallographic directions in alloys such as $Ti_{78}Nb_{22}$, $Mn_{87}Cu_{13}$ and $Mn_{80}Ga_{20}$ (see Fig. 1(c) and Supplementary Table 1). Such lattice intrinsic $|\alpha_l|$ is expected to bring a macroscopic large $|\alpha_l|$ and consequently a large TeE in [100] or [001]-textured martensitic polycrystals. In the following, to demonstrate the large TeE enabled by large $|\alpha_l|$, we will fabricate [100]-textured $Ti_{78}Nb_{22}$ martensitic polycrystals by plastic deformation. The macroscopic α_l, elastic behavior, TeE, and heat-pumping energy efficiency of this material will then be examined.

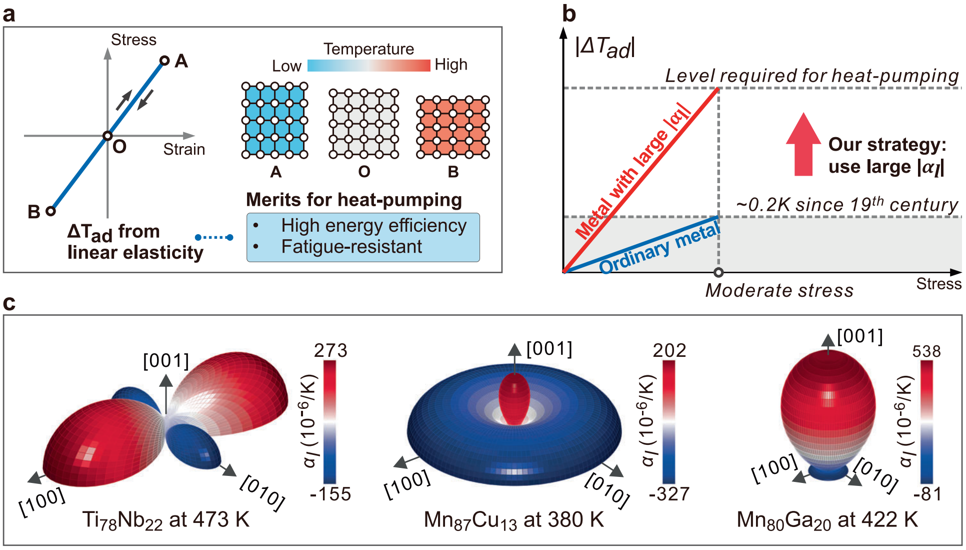

Fig. 1 | Key idea and candidate materials for obtaining large thermoelastic effect (TeE). a schematic illustration of the TeE of a solid possessing positive thermal expansion; within linear elastic regime (see blue line), the solid warms (or cools) when compressed (or stretched); the resulting adiabatic temperature change ΔT_{ad} is schematically shown using different colors. **b** schematic diagram showing large TeE (i.e., large $|\Delta T_{ad}|$ from elasticity) enabled by a large coefficient of linear thermal expansion $|\alpha_l|$; according to Eq. (1), the $|\Delta T_{ad}|$ is linearly proportional to applied stress; a large $|\alpha_l|$ causes a steep slope and thus a large $|\Delta T_{ad}|$ under a moderate stress level. **c** Orientation-dependent intrinsic α_l of the martensitic lattice in $Ti_{78}Nb_{22}$, $Mn_{87}Cu_{13}$ and $Mn_{80}Ga_{20}$ alloys (see Supplementary Table 1 for data of more alloys); large intrinsic $|\alpha_l|$ exists along [100] or [001] crystallographic directions, indicating a large macroscopic $|\alpha_l|$ and thus large TeE in the [100]/[001]-textured martensitic polycrystals.

[100]-texture in $Ti_{78}Nb_{22}$ martensitic polycrystals by plastic deformation

In general, the [100] orientation of martensitic $Ti_{78}Nb_{22}$ crystal can be converted from the [010] orientation through compression-induced variant reorientation mechanism, which maximizes the contraction accommodated along the compression axis[34,35]. Following this principle, we employed a two-step plastic deformation process involving cold rolling and compression (CRC) to create a [100]-type texture from a solution-treated $Ti_{78}Nb_{22}$ martensitic polycrystalline sample (Supplementary Fig. 3(a)). The initial solution-treated sample has near random orientations (Supplementary Fig. 3(b)), resulting in macroscopic isotropic small CTEs of ~10^{-5}/K (Supplementary Fig. 3(c))[30,36] and thus a weak TeE ($|\Delta T_{ad}|$ of ~0.3 K) (Supplementary Fig. 3(d)). Cold rolling selectively orients the rolling direction (RD) of the sample to the [010] crystal directions of the martensitic phase (Supplementary Fig. 4(a–c)). We made such [010] || RD texture strongest by using an optimized thickness reduction ratio of 50%[37]. However, limited by the intrinsic CTE along [010] (Supplementary Table 1), this rolling texture cannot lead to a large macroscopic CTE and TeE(Supplementary Fig. 4(d–f)). We reorient the rolling texture to the desired type of [100] || RD by uniaxially compressing the 50% cold-rolled sample along the RD (Supplementary Fig. 5(a)). Mediated through domain switching[38,39], such texture reorientation process finishes when the permanent strain reaches 14.4%, as reflected by the saturation of the resulting macroscopic CTE and TeE (Supplementary Fig. 5(b–e)). Thus, via CRC with an optimized 50% rolling thickness reduction and 14.4% plastic strain, we finally prepare polycrystalline $Ti_{78}Nb_{22}$ exhibiting a pronounced [100] || RD texture (Supplementary Fig. 5(d)) (hereafter referred to as [100]-textured $Ti_{78}Nb_{22}$).

The full martensitic phase composition of the [100]-textured $Ti_{78}Nb_{22}$ is verified using synchrotron x-ray diffraction (Supplementary Fig. 6). The microstructure consists of martensitic lamellae of around 5–10 nm wide and 30–50 nm long and martensitic grains of around 10–40 nm in size (Supplementary Fig. 7(a)). During heating to 473 K, the sample exhibits no discernible signal of martensite → austenite transition. This is evidenced by the overall stable microstructure and electron-diffraction pattern characterized by in-situ heating TEM (Supplementary Fig. 7(b–d)), absence of discernible austenite peaks in in-situ x-ray diffractograms (Fig. 2(a)), and absence of an exothermic phase-transition peak in heat flow curve (Fig. 2(b))[40,41]. Local microstructure changes with heating are detected by in-situ TEM (see circled regions in Supplementary Fig. 7(b–d)), consistent with the relative intensity changes of the martensite 020 and 002 peaks in in-situ x-ray diffractograms (Fig. 2(a)). These local microstructure changes are not from reverse phase transition since the crystal structure in the corresponding region remains orthorhombic, as evidenced by in-situ high-resolution TEM (Supplementary Fig. 7(e–h)). Instead, they are from the local lattice distortion of the orthorhombic martensite induced by residual and thermal stresses, as indicated by the lattice elastic strains in Supplementary Fig. 7(f, h).

For the non-phase-transforming [100]-textured martensitic $Ti_{78}Nb_{22}$, the measured macroscopic thermal expansion (Supplementary Fig. 5(e)) is simply from the lattice thermal expansion of the martensite[30,42–45]. This lattice-level behavior is evidenced by the shifting of X-ray diffraction peak (Fig. 2(a)), moving leftwards (or rightwards) for the crystal orientations exhibiting positive (or negative) CTEs. Due to the strong [100] || RD texture, the lattice CTE along [100] makes the major contribution to the macroscopic CTE along the RD. As the lattice CTE increases with temperature (Eq. (2)), the macroscopic CTE along the RD rises from $(26 \pm 3) \times 10^{-6}\,K^{-1}$ (averaged over three samples) near 300 K to $(94 \pm 9) \times 10^{-6}\,K^{-1}$ near 473 K (Fig. 2(c)), reaching one-third of the lattice CTE ($+273 \times 10^{-6}\,K^{-1}$).

The [100]-textured $Ti_{78}Nb_{22}$ yields when compressed to 880 MPa at 298 K and 800 MPa at 473 K (Supplementary Fig. 8). In-situ synchrotron x-ray diffraction during compression (Fig. 2(e)) reveals no stress-induced martensite → austenite transition. The sample simply undergoes elastic deformation, as evidenced by the reversible shifting of the martensite diffraction peaks in loading and unloading. Under 750 MPa compressive stress, the [100]-textured $Ti_{78}Nb_{22}$ shows recoverable near-linear stress strain curves in the temperature range of 298 K to 473 K (Fig. 2(d)). Unusually, the [100]-textured $Ti_{78}Nb_{22}$ possesses a macroscopic CTE (α_l) resembling that of elastomers and polymers, along with a yield strength (σ_y) characteristic of metals. This results in a $\alpha_l \cdot \sigma_y$ that surpasses known materials by a factor of 10–10^4 (Supplementary Fig. 9). Such unusually large $\alpha_l \cdot \sigma_y$ ($\propto \Delta T_{ad}$, see Eq. (1)) underlies the large TeE of the [100]-textured $Ti_{78}Nb_{22}$, as shown below.

Observation of TeE in [100]-textured $Ti_{78}Nb_{22}$ martensitic polycrystals

We measured the ΔT_{ad} of the [100]-textured $Ti_{78}Nb_{22}$ in response to rapid release of 700 MPa compressive stress along the RD at temperatures from 298 K to 473 K. At 298 K, a relatively small $|\Delta T_{ad}|$ of (2.2 ± 0.2) K is observed owing to the small positive CTE (Fig. 3(a)). Elevating the ambient temperature augments the CTE (Fig. 2(c)), consequently amplifying the TeE (Fig. 3(a)). At 473 K, the $|\Delta T_{ad}|$ reaches (5.2 ± 0.2) K (averaged over four samples; see the results of another sample in Supplementary Fig. 10). This $|\Delta T_{ad}|$ far exceeds the values obtained at the elastic limits of common metallic materials (0.1–0.5 K), polymers (0.3–1.6 K), glasses and ceramics (0.03–0.23 K) (see Supplementary Table 2). At temperatures from 413 K to 473 K, the $Ti_{78}Nb_{22}$ shows a ΔT_{ad} of 4–5.2 K, which is a reasonable level for developing solid-state heat-pumping devices[19,46]. The measured ΔT_{ad} well agrees with the values (Fig. 3(b)) predicted using Eq. (1) and the measured temperature-dependent CTEs (Fig. 2(c)) and specific heat capacity λ (Supplementary Fig. 11). This agreement confirms that the observed caloric effect is indeed from elastic deformation of the martensitic phase, which is also supported by the lattice elasticity revealed in Fig. 2(e).

We examined the cyclic stability of the TeE in two [100]-textured $Ti_{78}Nb_{22}$ specimens under 700 MPa uniaxial compressive stress at 473 K (Fig. 3(c)). Over one thousand cycles of compression, we find no obvious ΔT_{ad} degradation in both specimens (Fig. 3(d)), though a residual strain of 0.5% (Fig. 3(c)) is accumulated owing to a small amount of plasticity. Such irreversible deformations predominantly occur in the initial one hundred cycles, and is eventually suppressed by the mechanical training effect, leading to a linear stress-strain curve with practically zero hysteresis loop area $(0.012 \pm 0.005$ MPa) (Fig. 3(c)). The long-term cyclic stability is further confirmed at 298 K (long-term fatigue at 473 K is constrained by experimental facilities) using a third specimen over 10 million compression cycles (Fig. 3(d)). The excellent cyclic stability of the ΔT_{ad} is in sharp contrast to the severe degradation in ΔT_{ad} of typical superelastic NiTi SMA under full phase transition (Fig. 3(d)).

We calculated the material-level coefficient of performance (COP_{mat}) of the [100]-textured $Ti_{78}Nb_{22}$ in a Stirling heat-pumping cycle by using a thermodynamic model in[47,48] (see Note 2 of Supplementary information) along with the measured properties of the $Ti_{78}Nb_{22}$ (see Supplementary Table 3). Under $T_c = 288$ K (heat source temperature) and $T_h = 298$ K (heat sink temperature), the $Ti_{78}Nb_{22}$ exhibits a COP_{mat} of 25.3, equivalent to a second law efficiency of 88% ($COP_{carnot} = T_c/(T_h - T_c) = 28.8$). As shown in Fig. 3(e), such efficiency well surpasses those from first-order phase transitions in electrocaloric materials (31–41%[47]) and elastocaloric SMAs (55–71%[47]) and rivals those from second-order phase transition in magnetocaloric materials (79–91%[47]) and liquid-vapor phase transition in commercial VC refrigerants (86–91%[47]). At high temperatures, the $Ti_{78}Nb_{22}$ has an even higher second-law efficiency of 94% (assuming $T_c = 468$ K and $T_h = 478$ K).

The [100]-textured $Ti_{78}Nb_{22}$ with high efficiency and large ΔT_{ad} at high temperatures can be used to develop energy-efficient heat pumps

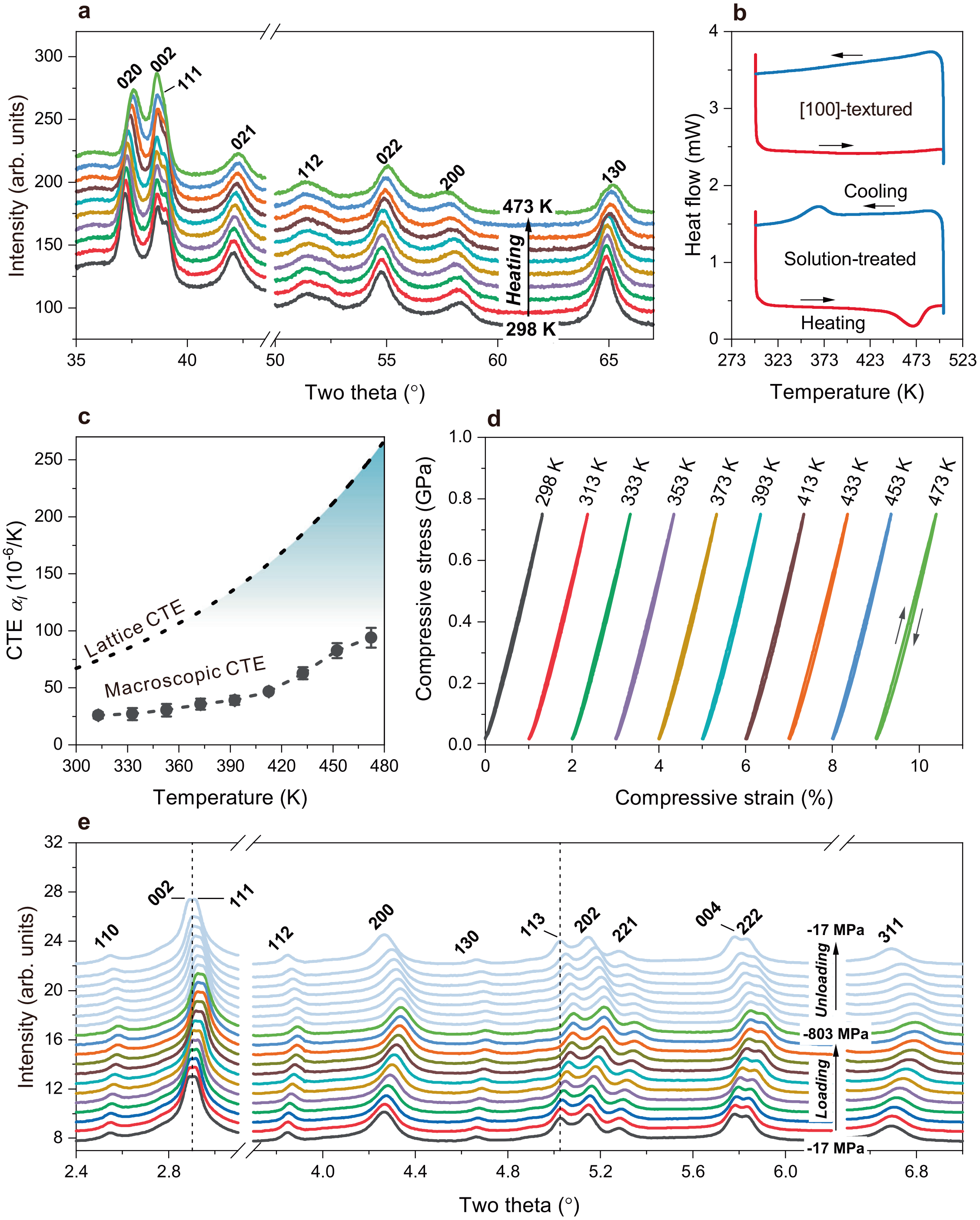

Fig. 2 | Thermal expansion and compressive elastic behavior of [100]-textured $Ti_{78}Nb_{22}$ martensitic polycrystals. **a** In-situ x-ray diffractograms measured during heating from 298 K to 473 K, showing absence of thermally induced reverse phase transition of the [100]-textured $Ti_{78}Nb_{22}$. Note that the relative intensities of the (020), (002), and (111) peaks change during heating. This is partly from the local microstructure changes, as revealed in Supplementary Fig. 7 by in-situ TEM, and partly from the apparent mergence of the (111) and (002) peaks due to anisotropic lattice thermal expansion. **b** Differential scanning calorimeter curves. **c** Temperature-dependent macroscopic coefficient of thermal expansion (CTE) measured along rolling direction (RD); the data is presented as mean values ± standard deviation over three distinct samples; for comparison, the lattice-level CTE (taken from ref. 49) along [100] crystallographic direction is also shown. **d** Isothermal compressive stress-strain curves under 750 MPa stress along the RD at different temperatures. **e** In-situ synchrotron x-ray spectra during compression along RD, showing lattice elasticity.

for industrial heat supply. In global industrial sector, heat supply in the temperature range of 373–503 K contributes to ~40% of total energy consumption[2–4]. A huge amount of coal and natural gas could be saved if this heat could be supplied using energy-efficient heat-pumping technologies. Compared to vapor-compression heat pumps, which mostly operate below 413 K[3], heat pumps using large TeE of the $Ti_{78}Nb_{22}$ can be more ecofriendly and supply heat to higher temperatures for wider industrial uses.

Prediction of TeE in martensitic single crystals

The large TeE of the [100]-textured $Ti_{78}Nb_{22}$ martensitic polycrystals was obtained by exploiting only 1/3 of the lattice intrinsic α_l. In

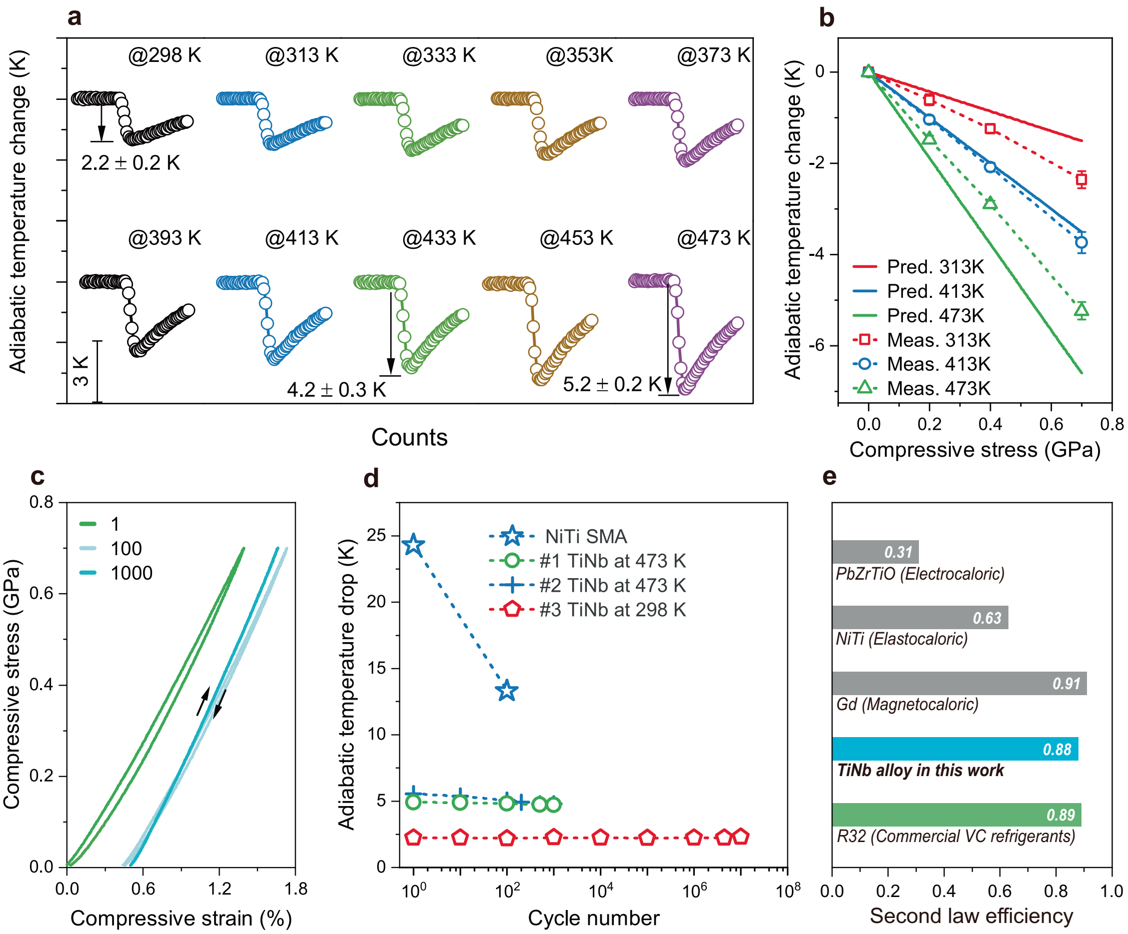

Fig. 3 | Observed thermoelastic effect (TeE) of [100]-textured $Ti_{78}Nb_{22}$ martensitic polycrystals. **a** Measured ΔT_{ad} upon rapid release of 700 MPa compressive stress along rolling direction at different temperatures. **b** Comparison between the predicted and measured ΔT_{ad}; the experimental data are presented as mean values ± standard deviation over four distinct samples. **c** Evolution of isothermal stress-strain curves during cyclic compression at 473 K. **d** Evolution of ΔT_{ad} during cyclic compression at 473 K and 298 K; two $Ti_{78}Nb_{22}$ samples (#1 and #2) were tested at 473 K to verify the repeatability; the data for typical NiTi shape memory alloy (SMA)[51] is also plotted for comparison. **e** Second law efficiency of the $Ti_{78}Nb_{22}$ and phase-transitional materials calculated under the same working condition of $T_c = 288$ K and $T_h = 298$ K; the values for phase-transition materials are taken from ref. 47 while that for the $Ti_{78}Nb_{22}$ is detailed in Note 2 of Supplementary Information.

martensitic single crystals of $Ti_{78}Nb_{22}$ and other ferroelastic alloys, the full intrinsic α_l can lead to larger TeE, as predicted below.

Using Eq. (1) and the measured lattice intrinsic α_l and λ (see Supplementary Table 1), we have calculated the ΔT_{ad} of ten types of martensitic single crystals under a moderate 500 MPa uniaxial stress applied along [100] or [001] directions. The calculation shows (see Fig. 4) that the intrinsic giant $|\alpha_l|$ of $(1.8–5.4) \times 10^{-4}$/K in these crystals can bring a large TeE with $|\Delta T_{ad}|$ of 9–22 K at a temperature of about 10 K below their respective A_s points (=155–480 K). As the temperature decreases, their $|\Delta T_{ad}|$ gradually diminishes, following the trend described by Eq. (3). The temperature window corresponding to $|\Delta T_{ad}| \geq 4$ K can reach tens of Kelvins (Fig. 4). Moreover, due to small hysteresis, the TeE can in principle produce high energy efficiency compared to typical first-order phase transitions. In experiment, the predicted large TeE of the single crystals can be approached in the respective polycrystals through generating [100] and [001] strong textures via tailored plastic deformation or via fabrication of column-grained specimens. Depending on their A_s point, the strongly textured martensitic alloys with large TeE can be used for energy-efficient heat-pumping and cooling at temperatures below, near or well above room temperature.

In summary, applying theory of thermoelasticity, we proved that the martensitic phase in ferroelastic alloys can indeed exhibit large thermoelastic effect when elastically stressed along its crystallographic direction of large intrinsic linear thermal expansion (α_l) near its absolute instability temperature. Guided by this prediction, we prepared [100]-textured martensitic $Ti_{78}Nb_{22}$ polycrystals by plastic deformation and obtained a large α_l of 94×10^{-6}/K. Under 700 MPa elastic compression, we achieved a large ΔT_{ad} of 4–5 K at temperatures of 413–473 K and a material-level high energy efficiency. Moreover, we identified ten types of single-crystalline ferroelastic alloys capable of exhibiting large $|\Delta T_{ad}|$ of 9–22 K under 500 MPa stress near their respective As temperature point (155–480 K). Our findings offer a non-phase-transition-based option for energy-efficient solid-state heat-pumping.

Methods

Materials preparation and plastic deformation

$Ti_{78}Nb_{22}$ button samples of 200 g were prepared from raw Ti and Nb elements of 99.9999% purity using an arc melting furnace in an Argon atmosphere. The samples were remelted five times to ensure chemical composition homogeneity. The as-melted samples were wire-cut into strips of 10 mm wide, 5 mm thick, and 40–50 mm long, and then sealed into quartz tubes under 99.999% purity argon and solution-treated at 1273 K for 25 h, followed by quenching into ice water. Differential scanning calorimetry (DSC) determined the transition temperatures of the solution-treated samples to be $M_s = 385$ K, $M_f = 339$ K, $A_s = 447$ K and $A_f = 486$ K, confirming a martensitic phase state (Cmcm crystal

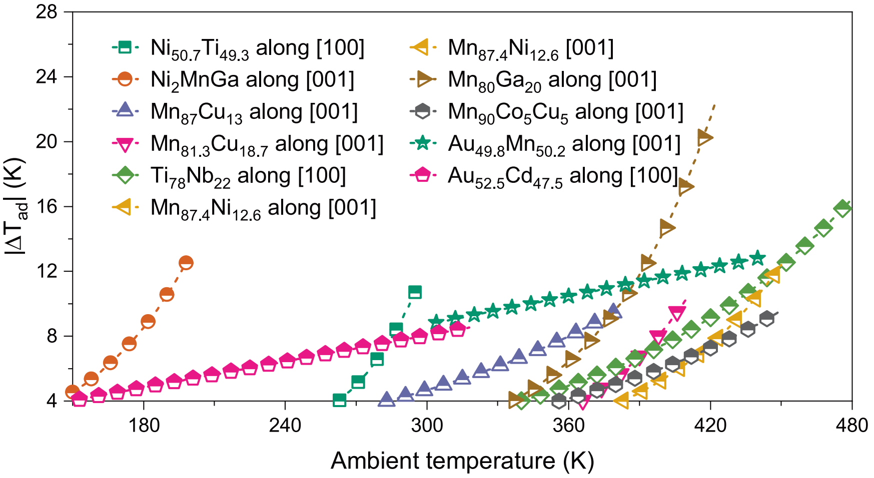

Fig. 4 | Predicted |ΔT_{ad}| in different martensitic single crystals under 500 MPa stress applied along [100] or [001] directions. The calculation is based on Eq. (1) as well as the experimental temperature-dependent lattice CTE (α_l) and heat capacity (λ) taken from the references in Supplementary Table 1. Note that for AuCd and AuMn alloys, the experimental data points for their temperature-dependent lattice parameters are too sparse to derive their temperature-dependent lattice CTEs; only the average lattice CTEs over a temperature range can be obtained and were used in the ΔT_{ad} calculation.

structure; $a = 3.1579$ Å, $b = 4.8422$ Å and $c = 4.6600$ Å[49]) at room temperature. To create a strong preferred orientation of RD || [010], the solution-treated $Ti_{78}Nb_{22}$ strips were rolled at room temperature at a low roller speed of 3 rpm, to 50% thickness reduction by 30 passes. Such low speed and small deformation increment allow rolling under an isothermal condition, avoiding thermally-induced austenite formation. Cuboid samples of 2.5 mm (|| TD) × 2.5 mm (|| ND) × 4 mm (|| RD) were cut using an electro-discharged machine from the 50% cold-rolled strips and then isothermally compressed along RD to 14.4% permanent strain on a material testing machine (MTS 858) at room temperature. After the cold-rolling and compression (CRC) processing, the samples were grinded to have a final dimension of 2.2 mm (|| TD) × 2.2 mm (|| ND) × 3.2 mm (|| RD).

Characterization of thermal expansion, elastic behavior, and thermoelastic effect

Macroscopic linear thermal expansion of solution-treated, as-rolled, and [100]-textured samples was measured along the RD during heating from 298 K to 473 K using a thermo-mechanical analyzer (NETZSCH TMA 402 F3) at a heating rate of 5 K/min. The temperature-dependent macroscopic CTEs of each sample are determined by least-square linear fitting of the measured macroscopic thermal expansion curve within a 20 K temperature window centered at each temperature point. The isothermal elastic deformation behavior of the [100]-textured sample to 750 MPa compressive stress was characterized using an Instron 5969 machine (equipped with a temperature chamber) under displacement control mode (0.08 mm/min) at ambient temperatures from 298 K to 473 K. The strain of the sample was recorded using a COD extensometer (EPSILO 3448-025M-020). The thermoelastic effect of the [100]-textured sample was measured through four steps: rapid loading at a stress rate of 5 GPa/s, constant stress holding for 15 s, rapid unloading at a stress rate of 10 GPa/s and zero-stress holding for 15 s. During this loading-unloading process, the sample temperature variations were synchronously measured using a data logger (NI-9212 DAQ) running at 100 Hz sampling frequency through a K-type thermocouple wire (80 µm diameter) spot welded onto the sample surface. The cyclic stability of the [100]-textured sample was tested to 10^3 compression cycles under 700 MPa at 473 K using the quasistatic Instron 5969 machine running at a frequency of 0.05 Hz and to 10^7 compression cycles under 750 MPa at 298 K using a dynamic MTS 858 machine running at a frequency of 20 Hz. During the cyclic test, we recorded the evolutions of the isothermal compressive stress-strain curve, ΔT_{ad} upon rapid unloading, and residual strain (determined from sample height change) of the [100]-textured sample.

Characterization of crystallographic texture

Using a Rigaku Smartlab x-ray diffractometer equipped with a 2D area detector, we characterized the crystallographic textures of the solution-treated, as-rolled, and [100]-textured samples with polished testing surfaces. For each sample, the pole figures for (022), (111), (113), and (202) reflections were measured within an α-angle range of 0° to 85° (with 5° increment) and a β-angle range of 0° to 360° (with 1° increment). From the pole figures, the orientation distribution function (ODF) was reconstructed under the assumption of orthorhombic sample symmetry and was used to calculate the inverse pole figures for RD, TD, and ND using MTEX package[50].

In-situ x-ray diffraction

To detect the lattice elastic deformation under compression, we performed in-situ high-energy X-ray diffraction measurements on the [100]-textured sample at beamline 11-ID-C in the Advanced Photon Source, Argonne National Laboratory (APS, ANL), USA. A monochromatic X-ray beam with energy 105.7 keV ($\lambda = 0.1173$ Å) and beam size of 500 µm (height) × 500 µm (width) was used. During compressive loading to 803 MPa, the x-ray diffractograms were measured using a 2-D detector placed ~1.7 m behind the sample at a frame frequency of 1 Hz.

In-situ high-temperature x-ray diffraction using Rigaku Smartlab diffractometer was carried out on the [100]-textured sample at temperatures from 298 K to 473 K (10 K apart). Nine cuboid samples of 1 mm × 2.2 mm × 3.2 mm in size were glued together and then polished to have a mirror-like large surface for the test. The samples were held for 10 min at each testing temperature to reach thermal equilibrium. X-ray diffractograms were measured using a spot size of ~2 mm in the two-theta angle range of 35° to 76° at a stepping rate of 2°/min.

In-situ transmission electron microscope

The in-situ TEM was performed using the chip-based heating inside a FEI Themis TEM at an electron accelerating voltage of 300 kV. The cross-sectional thin film sample was prepared by a FEI Helios Nanolab G3 dual-beam FIB using the standard lift-out procedures. The sample was precoated by e-beam induced Pt deposition before lift-out, and then mounted onto a DENSsolution heating chip with the supporting SiNx film milled off for better imaging conditions. The target area was polished with final voltage of 2 KV. The chip was loaded into the microscope right after the sample preparation.

Data availability

Source data are provided with this paper.

References

1. Zheng, X. et al. Characteristics of residential energy consumption in China: findings from a household survey. *Energy Policy* **75**, 126–135 (2014).
2. Commission, E. et al. *Potentials and levels for the electrification of space heating in buildings—Final report*. (Publications Office of the European Union, 2023).
3. Arpagaus, C., Bless, F., Uhlmann, M., Schiffmann, J. & Bertsch, S. S. High temperature heat pumps: market overview, state of the art, research status, refrigerants, and application potentials. *Energy* **152**, 985–1010 (2018).
4. Yan, H., Zhang, C., Shao, Z., Kraft, M. & Wang, R. The under-estimated role of the heat pump in achieving China's goal of carbon neutrality by 2060. *Engineering* **23**, 13–18 (2023).
5. Moya, X. & Mathur, N. D. Caloric materials for cooling and heating. *Science* **370**, 797 (2020).
6. Tušek, J. et al. A regenerative elastocaloric heat pump. *Nat. Energy* **1**, 1–6 (2016).
7. Greibich, F. et al. Elastocaloric heat pump with specific cooling power of 20.9 W g–1 exploiting snap-through instability and strain-induced crystallization. *Nat. Energy* **6**, 260–267 (2021).
8. Qian, S. et al. High-performance multimode elastocaloric cooling system. *Science* **380**, 722–727 (2023).
9. Zhou, G., Zhu, Y., Yao, S. & Sun, Q. Giant temperature span and cooling power in elastocaloric regenerator. *Joule* **7**, 2003–2015 (2023).
10. Ahčin, Ž. et al. High-performance cooling and heat pumping based on fatigue-resistant elastocaloric effect in compression. *Joule* **6**, 2338–2357 (2022).
11. Li, X., Hua, P. & Sun, Q. Continuous and efficient elastocaloric air cooling by coil-bending. *Nat. Commun.* **14**, 7982 (2023).
12. Bonnot, E., Romero, R., Mañosa, L., Vives, E. & Planes, A. Elastocaloric effect associated with the martensitic transition in shape-memory alloys. *Phys. Rev. Lett.* **100**, 125901 (2008).
13. Hou, H., Qian, S. & Takeuchi, I. Materials, physics and systems for multicaloric cooling. *Nat. Rev. Mater.* **7**, 633–652 (2022).
14. Chen, J., Xing, L., Fang, G., Lei, L. & Liu, W. Improved elastocaloric cooling performance in gradient-structured NiTi alloy processed by localized laser surface annealing. *Acta Materialia* **208**, 116741 (2021).
15. Chen, J. Toward tunable mechanical behavior and enhanced elastocaloric effect in NiTi alloy by gradient structure. *Acta Materialia* **226**, 117609 (2022).
16. Zhou, G. et al. A multi-material cascade elastocaloric cooling device for large temperature lift. *Nat. Energy* **9**, 862–870 (2024).
17. Zhou, G. et al. Achieving kilowatt-scale elastocaloric cooling by a multi-cell architecture. *Nature* **639**, 87–92 (2025).
18. Zhang, J., Cheng, S. & Sun, Q. Roller-cam-driven compressive elastocaloric device with high cooling power density. *Device*, https://doi.org/10.1016/j.device.2024.100677 (2025).
19. Hou, H. et al. Fatigue-resistant high-performance elastocaloric materials made by additive manufacturing. *Science* **366**, 1–6 (2019).
20. Thomson, W. On the thermoelastic, thermomagnetic, and pyro-electric properties of matter. *Lond. Edinb. Dublin Philos. Mag. J. Sci.* **5**, 4–27 (1878).
21. Joule, J. P. V. On some thermo-dynamic properties of solids. *Philos. Trans. R. Soc. Lond.* **149**, 91–131 (1859).
22. Nowacki, W. *Thermoelasticity*. (Elsevier, 2013).
23. Rocca, R. & Bever, M. B. The thermoelastic effect in iron and nickel as a function of temperature. *JOM* **2**, 327–333 (1950).
24. Candau, N., Vives, E., Fernández, A. I. & Maspoch, M. L. Elastocaloric effect in vulcanized natural rubber and natural/wastes rubber blends. *Polymer* **236**, https://doi.org/10.1016/j.polymer.2021.124309 (2021).
25. Zhang, S. et al. Solid-state cooling by elastocaloric polymer with uniform chain-lengths. *Nat. Commun.* **13**, 9 (2022).
26. Joule, J. P. & Thomson, W. XXII. On the thermal effects of longitudinal compression of solids. and On the alterations of temperature accompanying changes of pressure in fluids. *Proc. R. Soc. Lond.* **8**, 564–569 (1856).
27. Biot, M. A. Thermoelasticity and Irreversible Thermodynamics. *J. Appl. Phys.* **27**, 240–253 (1956).
28. Landau, L. D., Lifshitz, E. M., Kosevich, A. D. M. & Pitaevskii, L. P. *Theory of elasticity*. Vol. 7 (Elsevier, 1986).
29. Li, Q., Ahadi, A., Onuki, Y. & Sun, Q. Role of thermal expansion anisotropy on the elastocaloric effect of shape memory alloys with slim-hysteresis superelasticity. *Phys. Rev. Mater.* **7**, 013606 (2023).
30. Li, Q., Onuki, Y. & Sun, Q. Tailoring thermal expansion of shape memory alloys through designed reorientation deformation. *Acta Mater.* **218**, https://doi.org/10.1016/j.actamat.2021.117201 (2021).
31. Salje, E. *Phase transitions in ferroelastic and co-elastic crystals*. Vol. 104 (Cambridge University Press, 1990).
32. Barsch, G. R. & Krumhansl, J. A. Twin boundaries in ferroelastic media without interface dislocations. *Phys. Rev. Lett.* **53**, 1069–1072 (1984).
33. Falk, F. & Konopka, P. Three-dimensional Landau theory describing the martensitic phase transformation of shape-memory alloys. *J. Phys.: Condens. Matter* **2**, 61–77 (1990).
34. Shu, Y. C. & Bhattacharya, K. The influence of texture on the shape-memory effect in polycrystals. *Acta Mater.* **46**, 5457–5473 (1998).
35. Yu, C., Kang, G., Sun, Q. & Fang, D. Modeling the martensite reorientation and resulting zero/negative thermal expansion of shape memory alloys. *J. Mech. Phys. Solids* **127**, 295–331 (2019).
36. Gehring, D., Ren, Y., Barghouti, Z. & Karaman, I. In-situ investigation of anisotropic crystalline and bulk negative thermal expansion in titanium alloys. *Acta Mater.* **210**, 1–17 (2021).
37. Monroe, J. A. et al. Tailored thermal expansion alloys. *Acta Materialia* **102**, 333–341 (2016).
38. Bonisch, M., Calin, M., van Humbeeck, J., Skrotzki, W. & Eckert, J. Factors influencing the elastic moduli, reversible strains and hysteresis loops in martensitic Ti-Nb alloys. *Mater. Sci. Eng. C. Mater. Biol. Appl* **48**, 511–520 (2015).
39. Zhang, X., Wang, W., Sun, J., Gao, Y. & Pennycook, S. J. Enhanced twinning-induced plasticity effect by novel {315}α″/{332}β correlated deformation twins in a Ti-Nb alloy. *Int. J. Plast.* **148**, 103132 (2022).
40. Ahadi, A. & Sun, Q. Stress hysteresis and temperature dependence of phase transition stress in nanostructured NiTi—effects of grain size. *Appl. Phys. Lett.* **103**, 1–5 (2013).
41. Li, M. P. & Sun, Q. P. Nanoscale phase transition behavior of shape memory alloys — closed form solution of 1D effective modelling. *J. Mech. Phys. Solids* **110**, 21–37 (2018).
42. Ahadi, A., Matsushita, Y., Sawaguchi, T., Sun, Q. P. & Tsuchiya, K. Origin of zero and negative thermal expansion in severely-deformed superelastic NiTi alloy. *Acta Mater.* **124**, 79–92 (2017).
43. Li, Q. et al. In-plane low thermal expansion of NiTi via controlled cross rolling. *Acta Mater.* **204**, 1–14 (2021).
44. Li, Q., Onuki, Y., Ahadi, A. & Sun, Q. Large tunable thermal expansion in ferroelastic alloys by stress. *Acta Mater.* **240**, 118350 (2022).
45. Chu, K., Li, Q., Sun, Q. & Ren, F. Engineered colossal linear thermal expansion in nanocrystalline NiTi micropillars by stress. *Acta Mater.* **262**, https://doi.org/10.1016/j.actamat.2023.119442 (2024).
46. Wang, Y. et al. A high-performance solid-state electrocaloric cooling system. *Science* **370**, 129–133 (2020).

47. Qian, S. et al. Not-in-kind cooling technologies: a quantitative comparison of refrigerants and system performance. *Int. J. Refrig.* **62**, 177–192 (2016).
48. Qian, S. Thermodynamics of elastocaloric cooling and heat pump cycles. *Appl. Thermal Eng.* **219**, https://doi.org/10.1016/j.applthermaleng.2022.119540 (2023).
49. Bönisch, M. et al. Giant thermal expansion and α-precipitation pathways in Ti-alloys. *Nat. Commun.* **8**, 1–9 (2017).
50. Bachmann, F., Hielscher, R. & Schaeben, H. Texture Analysis with MTEX – Free and Open Source Software Toolbox. In *Solid State Phenomena*. Vol. 160 63–68 (Trans Tech Publ, 2010).
51. Chen, H. et al. Improvement of the stability of superelasticity and elastocaloric effect of a Ni-rich Ti-Ni alloy by precipitation and grain refinement. *Scr. Mater.* **162**, 230–234 (2019).

Acknowledgements

Q. Sun acknowledges financial support by the Hong Kong Research Grants Council through the RGC-STG Project No. STG2/E-605/23-N and RGC-GRF Project No. 16200324. B.B. He gratefully acknowledges the financial support from the National Natural Science Foundation of China (Grant No. 52471135), Science and Technology Innovation Commission of Shenzhen (Project No. JCYJ20210324120209026; KQTD2019092917250571), open research fund of Songshan Lake Materials Laboratory (2023SLABFK02), Major Talent Programs of Guangdong Province (Contract No. 2019QN01C435) and High Level of Special Funds (G03034K003) from SUSTECH. Y. Ren acknowledges the financial support by City University of Hong Kong (CityU 9610533). K. Chu acknowledges the financial support by the Guangdong Basic and Applied Basic Research Foundation (Grant no. 2025A1515011336) and the Shenzhen Science and Technology Program (Grant no. JCYJ20220530113015040).

Author contributions

Conceptualization: Q.L., Q.P.S. Methodology: Q.L., Z.Z.D., J.Y., K.C., K.H., S.H., Y.R. Investigation: Q.L., Z.Z.D., A.A., B.B.H., Q.P.S. Visualization: Q.L. Funding acquisition: B.B.H., Q.P.S. Supervision: Z.Z.D., B.B.H., Q.P.S. Writing—original draft: Q.L. Writing—review & editing: Q.L., Z.Z.D., A.A., B.B.H., Q.P.S.

Competing interests

The authors declare no competing interests.

Additional information

Supplementary information The online version contains supplementary material available at https://doi.org/10.1038/s41467-025-59720-3.

Correspondence and requests for materials should be addressed to Zhongzheng Deng, Binbin He or Qingping Sun.

Peer review information *Nature Communications* thanks the anonymous reviewer(s) for their contribution to the peer review of this work. A peer review file is available.

Reprints and permissions information is available at http://www.nature.com/reprints